

Structure Functions in the Decay $\tau^\mp \rightarrow \pi^\mp \pi^0 \pi^0 \nu_\tau$

CLEO Collaboration
(July 23, 2021)

Abstract

Using the CLEO II detector operating at the CESR e^+e^- collider, we have measured the structure functions in the decay $\tau^\mp \rightarrow \pi^\mp \pi^0 \pi^0 \nu_\tau$, based on a sample corresponding to 4×10^6 produced τ -pair events. We determine the integrated structure functions, which depend only on the three pion invariant mass, as well as the structure functions differential in the Dalitz plot. We extract model independent limits on non-axial-vector contributions from the measured structure functions as less than 16.6% of the total branching fraction, at the 95% confidence level. Separating the non-axial-vector contributions into scalar and vector contributions, we measure that scalars (vectors) contribute with less than 9.4% (7.3%) to the total branching ratio, at the 95% confidence level.

PACS numbers: 13.25.Jx, 13.35.Dx, 14.40.Cs, 14.60.Fg

T. E. Browder,¹ Y. Li,¹ J. L. Rodriguez,¹ H. Yamamoto,¹ T. Bergfeld,² B. I. Eisenstein,² J. Ernst,² G. E. Gladding,² G. D. Gollin,² R. M. Hans,² E. Johnson,² I. Karliner,² M. A. Marsh,² M. Palmer,² C. Plager,² C. Sedlack,² M. Selen,² J. J. Thaler,² J. Williams,² K. W. Edwards,³ R. Janicek,⁴ P. M. Patel,⁴ A. J. Sadoff,⁵ R. Ammar,⁶ P. Baringer,⁶ A. Bean,⁶ D. Besson,⁶ R. Davis,⁶ S. Kotov,⁶ I. Kravchenko,⁶ N. Kwak,⁶ X. Zhao,⁶ S. Anderson,⁷ V. V. Frolov,⁷ Y. Kubota,⁷ S. J. Lee,⁷ R. Mahapatra,⁷ J. J. O'Neill,⁷ R. Poling,⁷ T. Riehle,⁷ A. Smith,⁷ S. Ahmed,⁸ M. S. Alam,⁸ S. B. Athar,⁸ L. Jian,⁸ L. Ling,⁸ A. H. Mahmood,^{8,1} M. Saleem,⁸ S. Timm,⁸ F. Wappler,⁸ A. Anastassov,⁹ J. E. Duboscq,⁹ K. K. Gan,⁹ C. Gwon,⁹ T. Hart,⁹ K. Honscheid,⁹ H. Kagan,⁹ R. Kass,⁹ J. Lorenc,⁹ H. Schwarthoff,⁹ E. von Toerne,⁹ M. M. Zoeller,⁹ S. J. Richichi,¹⁰ H. Severini,¹⁰ P. Skubic,¹⁰ A. Undrus,¹⁰ M. Bishai,¹¹ S. Chen,¹¹ J. Fast,¹¹ J. W. Hinson,¹¹ J. Lee,¹¹ N. Menon,¹¹ D. H. Miller,¹¹ E. I. Shibata,¹¹ I. P. J. Shipsey,¹¹ Y. Kwon,^{12,2} A.L. Lyon,¹² E. H. Thorndike,¹² C. P. Jessop,¹³ K. Lingel,¹³ H. Marsiske,¹³ M. L. Perl,¹³ V. Savinov,¹³ D. Ugolini,¹³ X. Zhou,¹³ T. E. Coan,¹⁴ V. Fadeyev,¹⁴ I. Korolkov,¹⁴ Y. Maravin,¹⁴ I. Narsky,¹⁴ R. Stroynowski,¹⁴ J. Ye,¹⁴ T. Wlodek,¹⁴ M. Artuso,¹⁵ R. Ayad,¹⁵ E. Dambasuren,¹⁵ S. Kopp,¹⁵ G. Majumder,¹⁵ G. C. Moneti,¹⁵ R. Mountain,¹⁵ S. Schuh,¹⁵ T. Skwarnicki,¹⁵ S. Stone,¹⁵ A. Titov,¹⁵ G. Viehhauser,¹⁵ J.C. Wang,¹⁵ A. Wolf,¹⁵ J. Wu,¹⁵ S. E. Csorna,¹⁶ K. W. McLean,¹⁶ S. Marka,¹⁶ Z. Xu,¹⁶ R. Godang,¹⁷ K. Kinoshita,^{17,3} I. C. Lai,¹⁷ P. Pomianowski,¹⁷ S. Schrenk,¹⁷ G. Bonvicini,¹⁸ D. Cinabro,¹⁸ R. Greene,¹⁸ L. P. Perera,¹⁸ G. J. Zhou,¹⁸ S. Chan,¹⁹ G. Eigen,¹⁹ E. Lipeles,¹⁹ M. Schmidtler,¹⁹ A. Shapiro,¹⁹ W. M. Sun,¹⁹ J. Urheim,¹⁹ A. J. Weinstein,¹⁹ F. Würthwein,¹⁹ D. E. Jaffe,²⁰ G. Masek,²⁰ H. P. Paar,²⁰ E. M. Potter,²⁰ S. Prell,²⁰ V. Sharma,²⁰ D. M. Asner,²¹ A. Eppich,²¹ J. Gronberg,²¹ T. S. Hill,²¹ D. J. Lange,²¹ R. J. Morrison,²¹ T. K. Nelson,²¹ J. D. Richman,²¹ R. A. Briere,²² B. H. Behrens,²³ W. T. Ford,²³ A. Gritsan,²³ H. Krieg,²³ J. Roy,²³ J. G. Smith,²³ J. P. Alexander,²⁴ R. Baker,²⁴ C. Bebek,²⁴ B. E. Berger,²⁴ K. Berkelman,²⁴ F. Blanc,²⁴ V. Boisvert,²⁴ D. G. Cassel,²⁴ M. Dickson,²⁴ P. S. Drell,²⁴ K. M. Ecklund,²⁴ R. Ehrlich,²⁴ A. D. Foland,²⁴ P. Gaidarev,²⁴ R. S. Galik,²⁴ L. Gibbons,²⁴ B. Gittelman,²⁴ S. W. Gray,²⁴ D. L. Hartill,²⁴ B. K. Heltsley,²⁴ P. I. Hopman,²⁴ C. D. Jones,²⁴ D. L. Kreinick,²⁴ T. Lee,²⁴ Y. Liu,²⁴ T. O. Meyer,²⁴ N. B. Mistry,²⁴ C. R. Ng,²⁴ E. Nordberg,²⁴ J. R. Patterson,²⁴ D. Peterson,²⁴ D. Riley,²⁴ J. G. Thayer,²⁴ P. G. Thies,²⁴ B. Valant-Spaight,²⁴ A. Warburton,²⁴ P. Avery,²⁵ M. Lohner,²⁵ C. Prescott,²⁵ A. I. Rubiera,²⁵ J. Yelton,²⁵ J. Zheng,²⁵ G. Brandenburg,²⁶ A. Ershov,²⁶ Y. S. Gao,²⁶ D. Y.-J. Kim,²⁶ and R. Wilson²⁶

¹University of Hawaii at Manoa, Honolulu, Hawaii 96822

²University of Illinois, Urbana-Champaign, Illinois 61801

³Carleton University, Ottawa, Ontario, Canada K1S 5B6
and the Institute of Particle Physics, Canada

¹Permanent address: University of Texas - Pan American, Edinburg TX 78539.

²Permanent address: Yonsei University, Seoul 120-749, Korea.

³Permanent address: University of Cincinnati, Cincinnati OH 45221

- ⁴McGill University, Montréal, Québec, Canada H3A 2T8
and the Institute of Particle Physics, Canada
- ⁵Ithaca College, Ithaca, New York 14850
- ⁶University of Kansas, Lawrence, Kansas 66045
- ⁷University of Minnesota, Minneapolis, Minnesota 55455
- ⁸State University of New York at Albany, Albany, New York 12222
- ⁹Ohio State University, Columbus, Ohio 43210
- ¹⁰University of Oklahoma, Norman, Oklahoma 73019
- ¹¹Purdue University, West Lafayette, Indiana 47907
- ¹²University of Rochester, Rochester, New York 14627
- ¹³Stanford Linear Accelerator Center, Stanford University, Stanford, California 94309
- ¹⁴Southern Methodist University, Dallas, Texas 75275
- ¹⁵Syracuse University, Syracuse, New York 13244
- ¹⁶Vanderbilt University, Nashville, Tennessee 37235
- ¹⁷Virginia Polytechnic Institute and State University, Blacksburg, Virginia 24061
- ¹⁸Wayne State University, Detroit, Michigan 48202
- ¹⁹California Institute of Technology, Pasadena, California 91125
- ²⁰University of California, San Diego, La Jolla, California 92093
- ²¹University of California, Santa Barbara, California 93106
- ²²Carnegie Mellon University, Pittsburgh, Pennsylvania 15213
- ²³University of Colorado, Boulder, Colorado 80309-0390
- ²⁴Cornell University, Ithaca, New York 14853
- ²⁵University of Florida, Gainesville, Florida 32611
- ²⁶Harvard University, Cambridge, Massachusetts 02138

I. INTRODUCTION

The hadronic structure in the decays $\tau^\mp \rightarrow \pi^\mp \pi^\mp \pi^\pm \nu_\tau$ and $\tau^\mp \rightarrow \pi^\mp \pi^0 \pi^0 \nu_\tau$ has been the focus of several studies in recent years [1–5]. In most of these studies, models are employed to characterize the hadronic structure. As data samples have grown, revealing new and complex features, the models used have also become more complicated. For example, simple models assume the 3π mass spectrum in these decays can be described by a single resonance, the $a_1(1260)$ meson. DELPHI [3] found it necessary to include a radially excited a_1 meson, the a'_1 meson. Subsequently, CLEO [4], obtained a slightly improved description when including an a'_1 meson, but found that the most significant improvement came about from accounting for a threshold effect in the mass-dependence of the a_1 width due to the opening of the $a_1 \rightarrow K^* K$ decay channel. Similarly, models attributing structure in the 3π Dalitz plot distributions solely to decay amplitudes associated with $a_1 \rightarrow \rho\pi$ were found to be insufficient by ARGUS [2] and CLEO [4], who see indications of isospin zero contributions, from $f_2(1270)$, $f_0(1370)$ and $f_0(400 - 1200)$ (e.g., σ) meson production. The models used are not unique, as significant variations in their form and content can lead to similar features in the distributions of observable quantities. In addition, no model has so far given a fully satisfactory description of the data.

Thus, although the studies done so far have improved our knowledge, we still do not have a clear picture of the hadronic dynamics in τ decay to neutrino plus three pions. Furthermore, it is difficult to compare results from different experiments and draw additional conclusions since each analysis can only be interpreted in the context of the specific model(s) considered.

J. H. Kühn and E. Mirkes [6] have constructed a convenient approach for model independent studies through the determination of structure functions. In this approach, the kinematics of the three pions are studied in a particular reference frame. In this frame, contributions from the production of 3π systems with different spin-parity quantum numbers are separated into different structure functions, expressed in a completely model independent fashion. This approach also has the advantage that the features in the data are condensed into a compact form which can be used to test models, alone or in conjunction with data from other experiments. So far, only OPAL [5] has determined the structure functions, using the decay $\tau^\mp \rightarrow \pi^\mp \pi^\mp \pi^\pm \nu_\tau$. They obtained the first fully model independent measurement of the signed τ neutrino helicity as well as a model independent limit on non-axial-vector contributions.

Here, we present a measurement of the structure functions in the decay $\tau^\mp \rightarrow \pi^\mp \pi^0 \pi^0 \nu_\tau$, based on data collected with the CLEO II detector corresponding to 4×10^6 produced τ -pair events. The sample of selected events is essentially the same as the one used in our model dependent analysis. Consequently, we refer the reader to the article reporting on that work [4] for details common to both analyses.

The outline for the rest of the article is as follows. In the next section, we summarize the structure function formalism of Kühn and Mirkes [6] as applied to this decay mode. In Section III, we describe the CLEO II detector and the event selection criteria. The method used to determine the structure functions is discussed in Section IV, and the results are presented in Section V. The derived limits on non-axial-vector contributions are given in Section VI. In Section VII we describe the sources of systematic error. A summary and discussion of the results follows in Section VIII.

II. THE STRUCTURE FUNCTION FORMALISM

Following the conventions of ref. [6], we denote the momenta of the three pions by q_i^μ , with the momentum of the charged pion given by q_3^μ and the momenta of the two neutral pions by $q_{1,2}^\mu$ ($|\vec{q}_2| > |\vec{q}_1|$). The momentum of the total hadronic system is denoted by $Q^\mu = q_1^\mu + q_2^\mu + q_3^\mu$ and its invariant mass by $\sqrt{Q^2}$.

For the description of the hadronic physics within the context of the structure functions, it is convenient, as outlined in ref. [6], to introduce two reference frames $\mathcal{S}(x, y, z)$ and $\mathcal{S}'(x', y', z')$, both defined in the three pion rest frame. The two frames are transformed into each other via a rotation matrix parametrized by the three Euler angles α , β , and γ , as illustrated in Fig. 1. The orientation of the reference frame $\mathcal{S}(x, y, z)$ is such that the z -axis is parallel to the normal $n_\perp = (\vec{q}_1 \times \vec{q}_2)/|\vec{q}_1 \times \vec{q}_2|$ to the three pion decay plane and the x -axis is parallel to \vec{q}_3 , the flight direction of the third pion. The reference frame $\mathcal{S}'(x', y', z')$ has its z' -axis aligned with $n_L = -\vec{Q}/|\vec{Q}|$, *i.e.* the flight direction of the laboratory frame as seen from the three pion rest frame. Its azimuthal orientation is chosen such that n_τ , the unobservable flight direction of the τ lepton in the three pion rest frame, lies in the (x', z') plane.

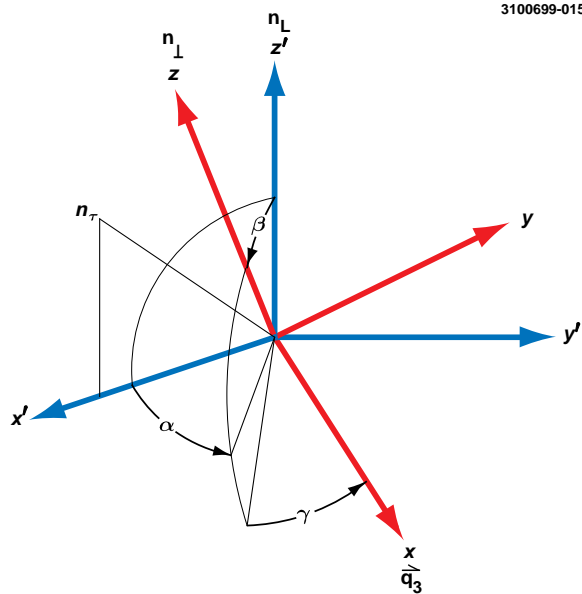


FIG. 1. Definition of the Euler angles α , β , and γ relating the two reference frames $\mathcal{S}(x, y, z)$ and $\mathcal{S}'(x', y', z')$, both defined in the three pion rest frame.

In the $\mathcal{S}(x, y, z)$ reference frame, using the structure functions W_X and the corresponding lepton tensor combinations \bar{L}_X of Kühn and Mirkes [6], the differential decay rate for $\tau^\mp \rightarrow \pi^\mp \pi^0 \pi^0 \nu$ can be written as follows [6]

$$d\Gamma(\tau \rightarrow 3\pi\nu_\tau) = C(Q^2) \sum_X \bar{L}_X(\alpha, \beta, \gamma, \theta_\tau, Q^2) W_X(Q^2, s_1, s_2) dQ^2 ds_1 ds_2 d\alpha d\gamma d\cos\beta d\cos\theta_\tau$$

$$\text{with } C(Q^2) = \frac{G_F^2}{4m_\tau(2\pi)^7 128} \cos^2\theta_c \frac{(m_\tau^2 - Q^2)^2}{m_\tau^2 Q^2}$$

$$\text{and } X \in \{A, B, \dots, I, SA, SB, \dots, SG\}, \quad (1)$$

where G_F is the Fermi constant, θ_c the Cabibbo angle, and s_i the Dalitz plot variables with $s_i = (q_j + q_k)^2$ ($i, j, k = 1, 2, 3; i \neq j \neq k$). The Euler angles α , β , and γ as well as the invariant mass $\sqrt{Q^2}$ of the three pion system have been introduced above. The angle θ_τ [6], which is the angle between the flight direction of the τ lepton in the laboratory system and the direction of the three pions in the τ lepton rest frame, is determined by the energy of the τ lepton in the laboratory frame, *i.e.* approximately half the energy of the incoming e^+e^- system, the energy of the three pion system in the laboratory frame, and the invariant mass of the three pion system. The sixteen structure functions W_X and the corresponding leptonic functions \bar{L}_X are symmetric and antisymmetric combinations of the hadron tensor $H^{\mu\nu}$ and, respectively, the lepton tensor $L^{\mu\nu}$. With the exception of the leptonic functions \bar{L}_A , \bar{L}_B , and \bar{L}_{SA} all leptonic functions \bar{L}_X vanish after integration over the angles α , β , γ , and θ_τ . Accordingly, the decay rate in a given bin of Q^2 or (Q^2, s_1, s_2) only depends on the structure functions W_A , W_B , and W_{SA} . For the details on the definitions of the structure functions W_X as well as the leptonic functions \bar{L}_X the reader is referred to ref. [6].

With the exception of the angle α , which determines the azimuthal orientation of the τ lepton, all variables in Eq. 1 are measurable quantities in our experiment. Accordingly, in this analysis we have to use the differential width $d\Gamma$ integrated over α . Performing this integral yields zero for the leptonic functions \bar{L}_{SC} , \bar{L}_{SE} , and \bar{L}_{SG} (see ref. [6]). Thus, in our experiment the corresponding structure functions W_{SC} , W_{SE} , and W_{SG} are not directly measurable.

Eq. 1 shows clearly the advantage of the chosen reference frame $\mathcal{S}(x, y, z)$. The structure functions W_X describing the hadronic physics depend on Q^2 , s_1 , and s_2 , only. The remaining dependence on the angular observables has been rotated into \bar{L}_X . Accordingly, measurement of the set of structure functions $W_X(Q^2, s_1, s_2)$ in the reference frame $\mathcal{S}(x, y, z)$ yields a model independent determination of the hadronic physics.

As mentioned above, the structure functions W_X are symmetric and antisymmetric combinations of the hadron tensor $H^{\mu\nu}$, which on the other hand is derived from the hadronic current h^μ by $H^{\mu\nu} = h^\mu h^{\nu*}$. In general h^μ is given by [6]

$$h^\mu = V_1^\mu F_1 + V_2^\mu F_2 + iV_3^\mu F_3 + V_4^\mu F_4, \quad (2)$$

where the form factors F_i describe the unknown hadronic physics and the vectors V_i^μ the known spin structure. A possible representation is

$$\begin{aligned} V_1^\mu &= q_1^\mu - q_3^\mu - Q^\mu \frac{(Q(q_1 - q_3))}{Q^2} \\ V_2^\mu &= q_2^\mu - q_3^\mu - Q^\mu \frac{(Q(q_2 - q_3))}{Q^2} \\ V_3^\mu &= \epsilon^{\mu\alpha\beta\gamma} q_{1\alpha} q_{2\beta} q_{3\gamma} \\ V_4^\mu &= q_1^\mu + q_2^\mu + q_3^\mu \equiv Q^\mu. \end{aligned} \quad (3)$$

The vectors $V_{1,2}^\mu$ correspond to an axial-vector intermediate hadronic state (*e.g.* the a_1 meson), V_3^μ to a vector intermediate hadronic state (*e.g.* the ρ' meson), and V_4^μ to a pseudoscalar or scalar intermediate hadronic state (*e.g.* the π' meson). Accordingly, the form factors $F_{1,2}$ describe axial-vector contributions, F_3 vector contributions, and F_4 pseudoscalar or scalar contributions. As can

be seen from Eq. 3, in the reference frame $\mathcal{S}(x, y, z)$ the hadronic current h^μ is decomposed into the time-like component h^0 induced by pseudoscalar or scalar contributions, the spatial components h^1 and h^2 by axial-vector contributions, and the spatial component h^3 by vector contributions. Table I summarizes the connection between the different J^P -states, *i.e.* the different components of the hadronic current h^μ in the reference frame $\mathcal{S}(x, y, z)$, and the structure functions W_X .

TABLE I. The different J^P -states and their connection with the sixteen structure functions W_X .

	$J = 0$ h^0	$J^P = 1^+$ h^1, h^2	$J^P = 1^-$ h^3
$J = 0$ h^{*0}	W_{SA}		
$J^P = 1^+$ h^{*1}, h^{*2}	W_{SB}, W_{SC} W_{SD}, W_{SE}	W_A W_C, W_D, W_E	
$J^P = 1^-$ h^{*3}	W_{SF}, W_{SG}	W_F, W_G W_H, W_I	W_B

The vector as well as the pseudoscalar contributions are suppressed due to G -Parity and PCAC. Nonetheless they can contribute. For example a possible reaction for the vector contribution in the charged pion mode is the decay chain $\tau^\mp \rightarrow \rho'^\mp \nu \rightarrow \pi^\mp \omega \nu$ with the ω meson decaying electromagnetically to two pions $\omega \rightarrow \pi^+ \pi^-$. Ref. [7] estimates that this decay contributes with 0.4% to the total $\tau^\mp \rightarrow \pi^\mp \pi^\mp \pi^\pm \nu$ decay rate, in agreement with the measured branching fraction of 0.6% [8]. In the neutral mode, $\tau^\mp \rightarrow \pi^\mp \pi^0 \pi^0 \nu$, vector contributions can occur via $\eta \pi^0$ mixing: $\tau^\mp \rightarrow \pi^\mp \pi^0 \eta \nu$ with the η meson transforming to a pion $\eta \rightarrow 2\gamma \rightarrow \pi^0$. The average of the measured branching fraction $\tau^\mp \rightarrow \pi^\mp \pi^0 \eta \nu$ from CLEO [9] and ALEPH [10] is $(0.17 \pm 0.03)\%$. Assuming the $\eta \pi^0$ mixing to be of the order of 10^{-2} , ref. [7] estimates the vector contribution in the neutral mode to be of the order of 10^{-5} .

States with $J = 0$ might occur via the π' intermediate state: $\tau^\mp \rightarrow \pi'^\mp \nu_\tau$. Assuming that the π' meson decays subsequently to $\rho\pi$ or $\sigma\pi$, CLEO [4] obtained the following upper limits: $\mathcal{B}(\tau \rightarrow \pi' \nu_\tau \rightarrow \rho\pi \nu_\tau \rightarrow 3\pi \nu_\tau) < 1.0 \times 10^{-4}$ and $\mathcal{B}(\tau \rightarrow \pi' \nu_\tau \rightarrow \sigma\pi \nu_\tau \rightarrow 3\pi \nu_\tau) < 1.9 \times 10^{-4}$ at the 90% confidence level.

Evidently, the sixteen structure functions W_X are not independent from each other. They are constructed from the hadronic current h^μ , which is determined by seven real numbers (an overall phase is redundant). Thus, there must exist nine relations among the sixteen structure functions. In general these relations are derived from

$$H_{\alpha\beta} \cdot H_{\gamma\delta} \equiv h^\alpha h^{*\beta} \cdot h^\gamma h^{*\delta} = h^\alpha h^{*\delta} \cdot h^\gamma h^{*\beta} \equiv H_{\alpha\delta} \cdot H_{\gamma\beta} \text{ for all } \{\alpha, \beta, \gamma, \delta\}. \quad (4)$$

Employing these relations enables one to deduce the structure functions W_{SC} , W_{SE} , and W_{SG} , despite the fact, as mentioned above, that the leptonic functions \bar{L}_{SC} , \bar{L}_{SE} , and \bar{L}_{SG} vanish after integration over the unobservable τ azimuth angle α .

III. DATA SAMPLE AND EVENT SELECTION

The analysis described here is based on 4 fb^{-1} of e^+e^- collision data collected at center-of-mass energies $2E_{\text{beam}}$ of $\sim 10.6 \text{ GeV}$, corresponding to 4×10^6 reactions of the type $e^+e^- \rightarrow \tau^+\tau^-$. These data were recorded at the Cornell Electron Storage Ring (CESR) with the CLEO II detector [11] between 1990 and 1995.

A. The CLEO II Detector

CLEO II is a general-purpose large solid angle magnetic spectrometer and calorimeter. Charged particle tracking is accomplished with three concentric cylindrical devices: a six-layer straw tube array surrounding a beam pipe of radius 3.2 cm that encloses the e^+e^- interaction point (IP), followed by two co-axial drift chambers of 10 and 51 sense wire layers respectively. Barrel ($|\cos\theta| < 0.81$, where θ is the polar angle relative to the beam axis) and end cap scintillation counters used for triggering and time-of-flight measurements surround the tracking chambers. The calorimeter comprises 7800 CsI(Tl) crystals, arrayed in projective (toward the IP) and axial geometries in barrel and end cap sections respectively. The barrel crystals present 16 radiation lengths to photons originating from the IP.

Identification of $\tau^\mp \rightarrow \pi^\mp \pi^0 \pi^0 \nu_\tau$ decays relies heavily on the segmentation and energy resolution of the calorimeter for reconstruction of the π^0 's. The central portion of the barrel calorimeter ($|\cos\theta| < 0.71$) achieves energy and angular resolutions of σ_E/E (%) = $0.35/E^{0.75} + 1.9 - 0.1 E$ and σ_ϕ (mrad) = $2.8/\sqrt{E} + 1.9$, with E in GeV, for electromagnetic showers. The angular resolution ensures that the two clusters of energy deposited by the photons from a π^0 decay are resolved over the range of π^0 energies typical of the τ decay mode studied here.

The detector elements described above are immersed in a 1.5 Tesla magnetic field provided by a superconducting solenoid surrounding the calorimeter. Muon identification is accomplished with proportional tubes embedded in the flux return steel at depths representing 3, 5 and 7 interaction lengths of total material penetration at normal incidence.

B. Identification of Candidate $\tau^\mp \rightarrow \pi^\mp \pi^0 \pi^0 \nu_\tau$ Decays

The event selection is nearly identical to that used in our model dependent analysis [4] of the $\tau^\mp \rightarrow \pi^\mp \pi^0 \pi^0 \nu_\tau$ decay. Here, we summarize the main features of the event selection procedure. For additional details, the article describing the model dependent analysis [4] should be consulted.

To identify events as $\tau\tau$ candidates we require the decay of the τ^\pm (denoted as the ‘tagging’ decay) that is recoiling against our signal τ^\mp decay to be classified as $\bar{\nu}_\tau e^\pm \nu_e$, or $\bar{\nu}_\tau \mu^\pm \nu_\mu$. A track is identified as an electron if its calorimeter energy to track momentum ratio satisfies $0.85 < E/p < 1.1$ and if its specific ionization in the main drift chamber is not less than 2σ below the value expected for electrons. It is classified as a muon if the track has penetrated to at least the innermost layer of muon chambers at 3 interaction lengths. Thus, we select events that contain two oppositely charged barrel tracks ($|\cos\theta| < 0.81$) with momenta between $0.08 E_{\text{beam}}$ and $0.90 E_{\text{beam}}$ and separated in angle by at least 90° , of which one track must be identified as an electron or muon.

Clusters of energy deposition in the central region of the calorimeter ($|\cos\theta| < 0.71$) that are not matched with a charged track projection are paired to form π^0 candidates. These showers

TABLE II. The four dominant background sources. The total background contribution is 12.6% leaving an additional 0.2% background contribution due to multiple sources not listed here.

fake π^0	$\tau^\mp \rightarrow \pi^\mp 3\pi^0 \nu_\tau$	$\tau^\mp \rightarrow K^\mp \pi^0 \pi^0 \nu_\tau$	$\tau^\mp \rightarrow K_S \pi^\mp \nu_\tau$
$(8.3 \pm 0.2)\%$	$(3.2 \pm 0.2)\%$	$(0.5 \pm 0.1)\%$	$(0.4 \pm 0.1)\%$

must have energies greater than 50 MeV, and the invariant mass of the photon-pair must lie within 7.5σ of the π^0 mass where σ varies between $\sim 4 - 7$ MeV. Those π^0 candidates with energy above $0.06 E_{\text{beam}}$ after application of a π^0 mass constraint are associated with any track within 90° .

A $\pi^\mp \pi^0 \pi^0$ candidate is formed from a track which has two associated π^0 candidates as defined above. If more than one combination of π^0 candidates can be assigned to a given track, only one combination is chosen: namely, that for which the largest unused barrel photon-like cluster in the $\pi^\mp \pi^0 \pi^0$ hemisphere has the least energy. A cluster is defined to be photon-like if it satisfies a 1% confidence level cut on the transverse shower profile and lies at least 30 cm away from the nearest track projection.

To ensure that these classifications are consistent with expectations from τ decay, events are vetoed if any unused photon-like cluster with $|\cos\theta| < 0.95$ has energy greater than 200 MeV, or if any unmatched non-photon-like cluster has energy above 500 MeV. The missing momentum as determined using the $\pi^\mp \pi^0 \pi^0$ and tagging systems must point into a high-acceptance region of the detector ($|\cos\theta_{\text{miss}}| < 0.9$), and must have a component transverse to the beam of at least $0.06 E_{\text{beam}}$.

Finally, we define the $\pi^0 \pi^0$ signal region to be that where the normalized invariant masses of the two photon-pairs, $S_{\gamma\gamma} \equiv (M_{\gamma\gamma} - m_{\pi^0})/\sigma_{\gamma\gamma}$, satisfies $-3.0 < S_{\gamma\gamma} < 2.0$ for both π^0 candidates. To estimate the contributions from fake π^0 's, we also define side and corner band regions using $-7.5 < S_{\gamma\gamma} < -5.0$ and $3.0 < S_{\gamma\gamma} < 5.5$. The final sample consists of 15849 events in the $\pi^0 \pi^0$ signal region. The side and corner band regions contain 1667 and 296 events, respectively.

The dominant backgrounds are due to mis-identification of τ decays to other final states. These background modes include (1) decays such as $\tau^\mp \rightarrow \pi^\mp \pi^0 \nu_\tau$ in which a spurious π^0 is reconstructed primarily from secondary clusters arising from interaction of the charged pion in the calorimeter, (2) decay modes with three or more π^0 's, in which the photons associated with the extra π^0 are not detected, (3) the Cabibbo-suppressed decay $\tau^\mp \rightarrow K^\mp \pi^0 \pi^0 \nu_\tau$, and (4) the mode $\tau^\mp \rightarrow \pi^\mp K_S^0 \nu_\tau$, in which the π^0 's originate via the $K_S \rightarrow \pi^0 \pi^0$ decay. The level of contamination from these background sources is given in Table II.

IV. METHOD

In our model dependent analysis [4], where we were only interested in the relative contributions of the amplitudes considered, we used a single entry maximum likelihood fit. Here, we extend the single entry maximum likelihood by the normalization to measure the absolute rate in a given bin of Q^2 as well as (Q^2, s_1, s_2) . As mentioned in section I these rates are determined by the structure functions W_A , W_B , and W_{SA} .

The likelihood in a given bin j of Q^2 or (Q^2, s_1, s_2) can be written as follows

$$-2 \ln \mathcal{L}_j = \sum_i^{N_{evt,j}} \left[-2 \ln \sum_X \left\{ \begin{array}{c} \tilde{L}_X W_X(Q^2, s_1, s_2) \\ \tilde{L}_X w_X(Q^2) \end{array} \right\} \right] + 2N_j, \quad (5)$$

where $N_{evt,j}$ is the number of events in bin j , and N_j the normalization of bin j . The upper expression in the braces in Eq. 5 is used in the determination of the structure functions W_X differential in the Dalitz plot, and the lower expression for the determination of the structure functions w_X integrated over the Dalitz plot. The leptonic functions \tilde{L}_X are integrated over the unobservable τ lepton azimuthal angle α including the τ pair production P and the factorized initial state radiation f_{ini}

$$\tilde{L}_X(\beta, \gamma, \theta_\tau, Q^2) = \int f_{ini}(\vec{\kappa}) \cdot P \cdot \bar{L}_X(\alpha, \beta, \gamma, \theta_\tau, Q^2) d\vec{\kappa} d\alpha, \quad (6)$$

where $\vec{\kappa}$ is the momentum of the radiated photon. For the initial state photon spectrum f_{ini} we use the formula obtained in ref. [12]. Overall constant factors of the τ pair production have been factored out and, accordingly, P denotes only the functional form of the τ pair production with $P = (1 + \cos^2 \theta_{\tau\tau})/2$, where $\theta_{\tau\tau}$ is the polar angle of the τ lepton with respect to the beam axis. The integrals over α and $\vec{\kappa}$ in Eq. 6 are evaluated numerically.

We have included the initial state bremsstrahlung in the leptonic functions \tilde{L}_X to account for the fact that the τ energy E_τ in the laboratory frame, needed for the evaluation of the angle θ_τ (Eq. 1), is in general not given by $E_\tau = \sqrt{s}/2$ but by $E_\tau = \sqrt{s'}/2$, where $\sqrt{s'}$ is the center of mass energy after radiation.

The inclusion of the τ pair production corrects for the fact that the $(1 + \cos^2 \theta_{\tau\tau})$ distribution of the τ leptons induces an anisotropic distribution of the τ momenta that lie on a cone around the three pion momentum. Azimuth angles that result in τ momenta closer to the beam are preferred over azimuth angles further away from the beam. In the absence of any selection cuts this anisotropy vanishes after integration over the orientation of the τ lepton or, equivalently, the orientation of the three pion system in the laboratory frame. However, the selection cuts applied yield a residual anisotropy affecting the leptonic functions \bar{L}_X .

Monte Carlo studies showed that the neglect of the τ pair production as well as of the initial state radiation results in a bias in the determination of the structure functions. In both cases the bias obtained is around 2%. Although the statistical uncertainty in our results is much larger than the effect of τ pair production, we expect that future analyses will not be limited by statistics and that pair production dynamics will be more important.

For a given bin j in Q^2 or in (Q^2, s_1, s_2) the normalization N_j in Eq. 5 is chosen to be

$$N_j = \frac{N_{evt}}{f_{sel}\Gamma} \times \tilde{\Gamma}_j = \frac{N_{evt}}{f_{sel}\Gamma} \times C(Q^2) \sum_X \int \left\{ \begin{array}{c} \tilde{L}_X W_X(Q^2, s_1, s_2) \\ \tilde{L}_X w_X(Q^2) \end{array} \right\} d\gamma d \cos \beta d \cos \theta_\tau, \quad (7)$$

where β , γ , θ_τ , and $C(Q^2)$ have been introduced above (see Eq. 1). The total number of events is denoted by N_{evt} . The partial width, Γ , of the τ^\mp lepton decaying into $\pi^\mp \pi^0 \pi^0 \nu_\tau$ is given by the total width $\Gamma_{tot} = \hbar/\tau_\tau$ times the branching fraction $\mathcal{B}(\tau^\mp \rightarrow \pi^\mp \pi^0 \pi^0 \nu_\tau)$. We use the world average values of $\Gamma_{tot} = (2.27 \pm 0.01) \times 10^{-3}$ eV [14] and $\mathcal{B}(\tau^\mp \rightarrow \pi^\mp \pi^0 \pi^0 \nu_\tau) = (9.15 \pm 0.15)\%$ [14] to determine the partial width Γ . The factor $f_{sel} = 0.996$ corrects for events that are outside of our selected region of $0.5 \text{ GeV}^2/c^4 < Q^2 < 2.75 \text{ GeV}^2/c^4$, *i.e.* $\sum_j \tilde{\Gamma}_j = f_{sel} \times \Gamma$.

As in our model dependent analysis [4], we account for the four main background sources, listed in Table II, by extending the likelihood of Eq. 5 as follows

$$\begin{aligned} \mathcal{L} = & (1 - \alpha_{f_{\pi^0}} - \alpha_{4\pi} - \alpha_{K\pi\pi} - \alpha_{K_S\pi}) \mathcal{L}_{signal} \\ & + \alpha_{f_{\pi^0}} \mathcal{L}_{f_{\pi^0}} + \alpha_{4\pi} \mathcal{L}_{4\pi} + \alpha_{K\pi\pi} \mathcal{L}_{K\pi\pi} + \alpha_{K_S\pi} \mathcal{L}_{K_S\pi}, \end{aligned} \quad (8)$$

where \mathcal{L}_{signal} is the likelihood of the signal events, $\mathcal{L}_{f_{\pi^0}}$ the likelihood of the fake π^0 background, $\mathcal{L}_{4\pi}$ the likelihood of the $\tau^\mp \rightarrow \pi^\mp(3\pi^0)\nu_\tau$ background, $\mathcal{L}_{K\pi\pi}$ the likelihood of the $\tau^\mp \rightarrow K^\mp\pi^0\pi^0\nu_\tau$ background, and $\mathcal{L}_{K_S\pi}$ the likelihood of the $\tau^\mp \rightarrow K_S\pi^\mp\nu_\tau$ background. The corresponding background fractions α_i are given by Table II. The likelihood $\mathcal{L}_{f_{\pi^0}}$ of the fake pion background is approximated by the Dalitz plot distributions of events populating the π^0 mass side bands. We model the likelihood $\mathcal{L}_{4\pi}$ of the four pion background with the decay $\rho(1450) \rightarrow \rho\sigma$ using a S -wave amplitude. To estimate the systematic error arising from the large theoretical and experimental uncertainties of the four pion matrix element we also consider the decay $\rho(1450) \rightarrow a_1\pi$ (S -wave). The integration over the lost π^0 meson, needed for the evaluation of $\mathcal{L}_{4\pi}$, is done numerically taking into account efficiency. The background $\tau^\mp \rightarrow K^\mp\pi^0\pi^0\nu_\tau$ is modeled by the decay chain $\tau^\mp \rightarrow K_1^\mp\nu_\tau$, $K_1^\mp \rightarrow K^{*\mp}\pi^0$ (S -wave), where the K_1 meson is parametrized by a superposition of the $K_1(1270)$ and $K_1(1400)$ Breit Wigner functions. Finally, the $\tau^\mp \rightarrow K_S\pi^\mp\nu_\tau$ background is parametrized by the decay chain $\tau^\mp \rightarrow K^{*\mp}\nu_\tau$, $K^{*\mp} \rightarrow K_S^0\pi^\mp$ (P -wave). The mass distribution for the $K_S \rightarrow \pi^0\pi^0$ decay is parametrized by a Gaussian, where the mean and the width are taken from data.

To determine the structure function integrated over the Dalitz plot we subdivide our data sample in nine equidistant bins of Q^2 . The considered Q^2 range is $0.50 \text{ GeV}^2/c^4 < Q^2 < 2.75 \text{ GeV}^2/c^4$ yielding a bin width of $0.25 \text{ GeV}^2/c^4$. In each of the nine bins we fit for the integrated structure functions w_A , w_C , w_D , and w_E . In this case non-axial-vector contributions are not taken into consideration, since, due to the loss of information by integrating over the Dalitz plot, we are unable to resolve these contributions.

Table III shows in detail the binning in (Q^2, s_1, s_2) used to extract the structure functions W_X differential in the Dalitz plot. In total we have 34 bins. Instead of fitting directly for the structure functions W_X and employing explicitly the nine relations among the structure functions (see Eq. 4), we introduce in each bin of (Q^2, s_1, s_2) seven fit parameters: the real $\Re(h_0)$ and imaginary part $\Im(h_0)$ of the time-like component of the hadronic current h^μ , the real part $\Re(h_1)$ of the x -component, the real $\Re(h_2)$ and imaginary part $\Im(h_2)$ of the y -component, and the real $\Re(h_3)$ and imaginary part $\Im(h_3)$ of the z -component. The imaginary part of the x -component $\Im(h_1)$ is chosen to be zero. From the measured hadronic current h^μ in a given bin of (Q^2, s_1, s_2) we then calculate the structure functions W_X taking into account the full covariance matrix for the error evaluation of the structure functions W_X .

V. MEASUREMENT

The fit results obtained for the integrated structure functions w_A , w_C , w_D , and w_E in comparison with the model obtained in our model dependent analysis [4] as well as the model of J. H. Kühn and A. Santamaria [13] (KS) are shown in Fig. 2. The observed steep falling of the structure function w_A around $Q^2 = 2 \text{ GeV}^2/c^4$, which might be an indication of the K^*K threshold opening, is well reproduced by the fit obtained in our model dependent analysis [4]. The KS-model [13], which does not include the K^*K threshold in the total width of the a_1 meson Breit Wigner function, falls less steeply around $Q^2 = 2 \text{ GeV}^2/c^4$, as can be seen from Fig. 2. Owing to the large statistical

TABLE III. Employed binning in (Q^2, s_1, s_2) as used in the fits differential in the Dalitz plot. The Dalitz plane is symmetrized with $s_1 > s_2$. Depending on s_1 , s_2^{max} is either given by the phase space boundaries (see *e.g.* ref. [14], section 35.4.3.1) or by the condition $s_1 > s_2$.

Bin	Q^2 [GeV ²]	s_1 [GeV ²]	s_2 [GeV ²]	N_j
1	0.50 – 0.75	0.00 – 0.35	0.00 – s_2^{max}	192
2		0.35 – 0.75	0.00 – s_2^{max}	204
3	0.75 – 1.00	0.00 – 0.48	0.00 – 0.32	527
4		0.48 – 0.56	0.00 – 0.32	575
5		0.56 – 1.00	0.00 – 0.32	492
6		0.32 – 0.68	0.32 – s_2^{max}	512
7	1.00 – 1.25	0.00 – 0.53	0.00 – 0.40	680
8		0.53 – 0.59	0.00 – 0.40	619
9		0.59 – 0.66	0.00 – 0.40	663
10		0.66 – 1.25	0.00 – 0.40	614
11		0.40 – 0.56	0.40 – s_2^{max}	645
12		0.56 – 0.85	0.40 – s_2^{max}	667
13	1.25 – 1.50	0.00 – 0.56	0.00 – 0.52	667
14		0.56 – 0.64	0.00 – 0.52	675
15		0.64 – 0.74	0.00 – 0.52	643
16		0.74 – 1.50	0.00 – 0.52	663
17		0.52 – 0.66	0.52 – s_2^{max}	665
18		0.66 – 0.98	0.52 – s_2^{max}	640
19	1.50 – 1.75	0.00 – 0.61	0.00 – 0.57	496
20		0.61 – 0.73	0.00 – 0.57	481
21		0.73 – 0.89	0.00 – 0.57	442
22		0.89 – 1.75	0.00 – 0.57	440
23		0.57 – 0.77	0.57 – s_2^{max}	490
24		0.77 – 1.18	0.57 – s_2^{max}	498
25	1.75 – 2.00	0.00 – 0.72	0.00 – 0.66	382
26		0.72 – 1.00	0.00 – 0.66	379
27		1.00 – 2.00	0.00 – 0.66	360
28		0.66 – 1.34	0.66 – s_2^{max}	373
29	2.00 – 2.25	0.00 – 1.05	0.00 – s_2^{max}	320
30		1.05 – 2.25	0.00 – s_2^{max}	300
31	2.25 – 2.50	0.00 – 1.25	0.00 – s_2^{max}	109
32		1.25 – 2.50	0.00 – s_2^{max}	124
33	2.50 – 2.75	0.00 – 1.20	0.00 – s_2^{max}	55
34		1.20 – 2.75	0.00 – s_2^{max}	47

errors obtained on the structure functions w_C , w_D , and w_E the comparison of the fit results and the models is not very conclusive for those three functions.

The fit results for the axial-vector part of the hadronic current (Table I) in bins of (Q^2, s_1, s_2) are shown in Fig. 3. The measured non-axial-vector contributions of the hadronic current are plotted in Fig. 4.

As mentioned in section IV, we derive the structure function W_X differential in the Dalitz plot

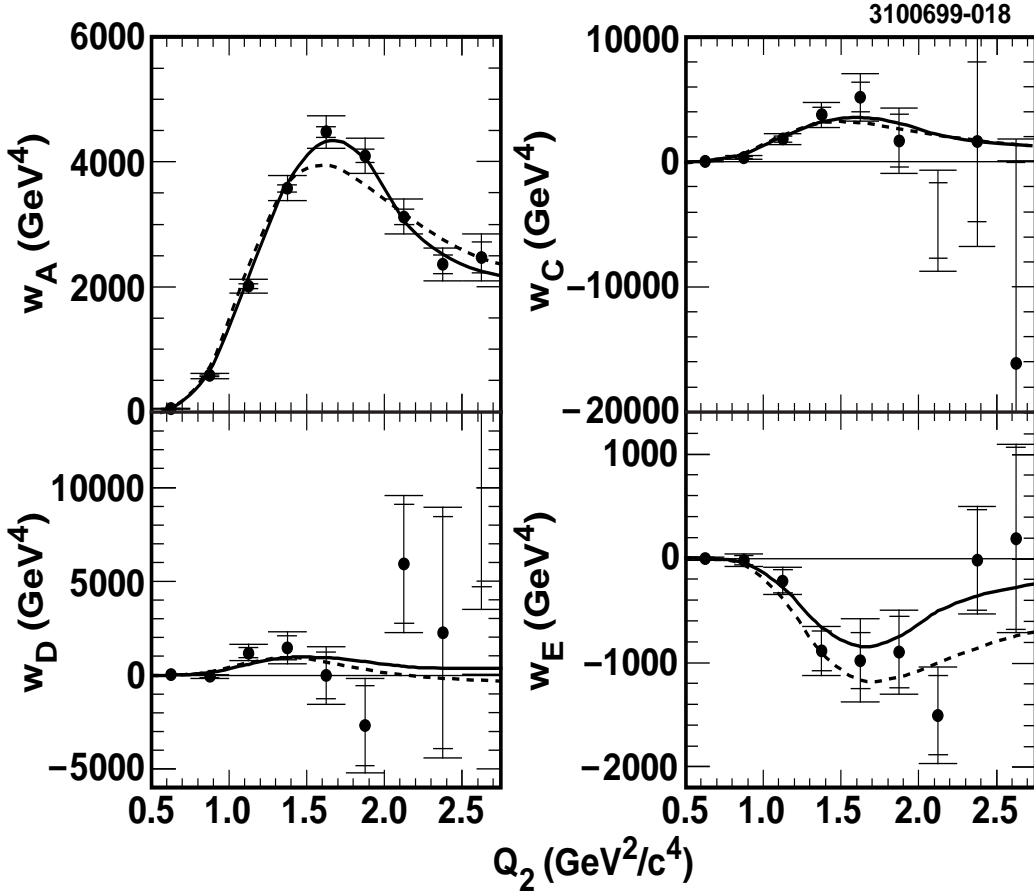


FIG. 2. The integrated structure functions w_A , w_C , w_D , and w_E . The filled points represent the data. The smaller error bars indicate the statistical errors. The distance between the smaller and larger error bars shows the systematic errors (see Section VII). The solid line is the model as obtained in our model dependent analysis, whereas the dotted line corresponds to the KS-model.

from our measured hadronic current including the full covariance matrix. The results obtained on the axial-vector induced structure functions W_A , W_C , W_D , and W_E are shown in Fig. 5, whereas Fig. 6 shows the non-axial-vector structure functions W_B , W_{SA} , W_{SF} , and W_{SG} . The structure functions that have their origin in the interference between the vector and axial-vector contributions of the hadronic current as well as the ones due to the interference between the scalar and axial-vector components of the hadronic current are plotted in Figs. 7 and 8, respectively.

The KS-model [13], as can be seen from Fig. 3, fails to describe the details of the hadronic current components $\Re(h_1)$ and $\Re(h_2)$. This discrepancy between the data and the KS-model [13] is also reflected in the functions W_A and W_C , shown in Fig. 5.

As illustrated by Fig. 4 and, correspondingly, by the Figs. 6, 7, and 8, we do not measure significant scalar or vector contributions. The null hypotheses for scalar and vector contributions as well as for scalar and vector contribution combined yield in all three cases significances below three standard deviations.

Tables summarizing our results on the structure functions as well as on the hadronic current

components are available on the WWW⁴.

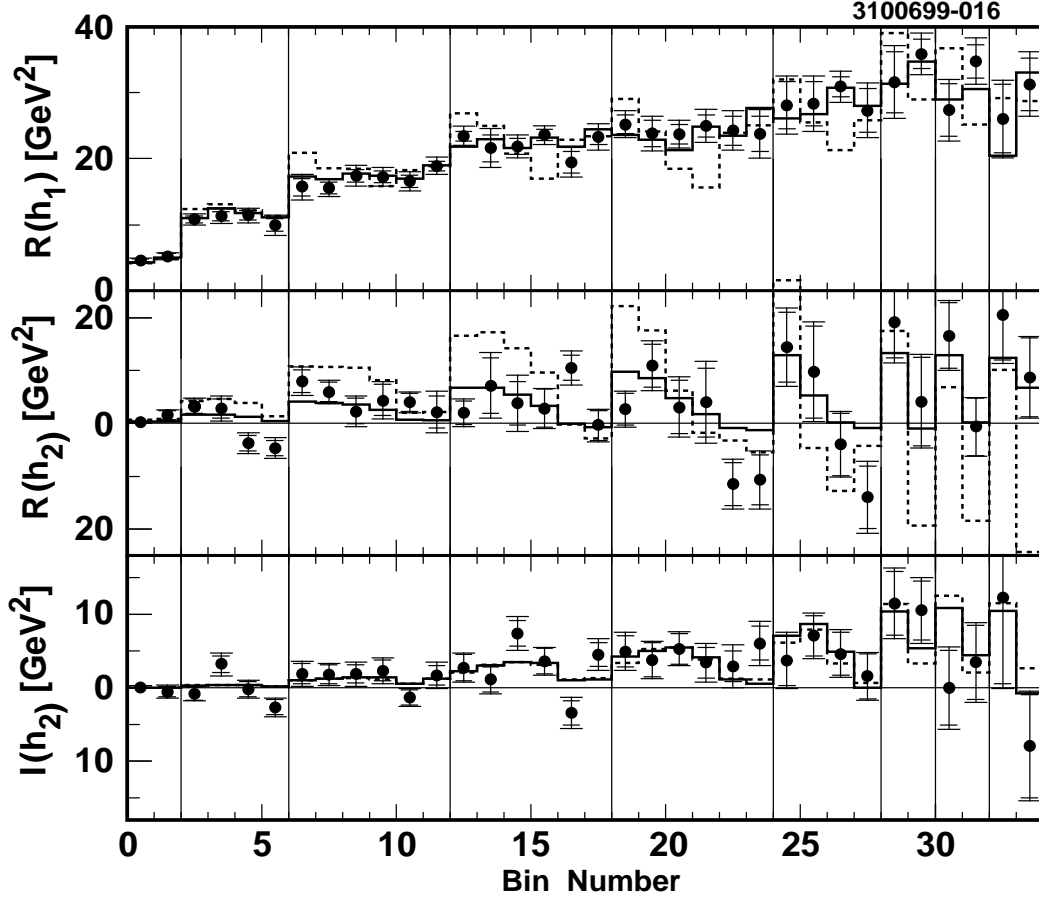


FIG. 3. The real and imaginary parts of the axial-vector induced components of the hadronic current as measured in our fits differential in the Dalitz plot. For the definition of the bin number the reader is referred to Table III. The filled points represent the data. The smaller error bars indicate the statistical errors. The distance between the smaller and larger error bars shows the systematic errors (see Section VII). The solid line is the model as obtained in our model dependent analysis, whereas the dotted line corresponds to the KS-model.

VI. LIMITS ON NON AXIAL-VECTOR CONTRIBUTION

The fit results on the scalar components of the hadronic current, *i.e.* the time-like components $\Re(h_0)$ and $\Im(h_0)$, yield the following branching fraction for scalar contributions

$$\frac{\mathcal{B}(\tau^\mp \rightarrow S\nu \rightarrow \pi^\mp \pi^0 \pi^0 \nu)}{\mathcal{B}(\tau^\mp \rightarrow \pi^\mp \pi^0 \pi^0 \nu)} = (5.2 \pm 2.5 \pm 0.3)\%, \quad (9)$$

⁴See <http://www.lns.cornell.edu/public/CLEO/analysis/results/tau-struct/>.

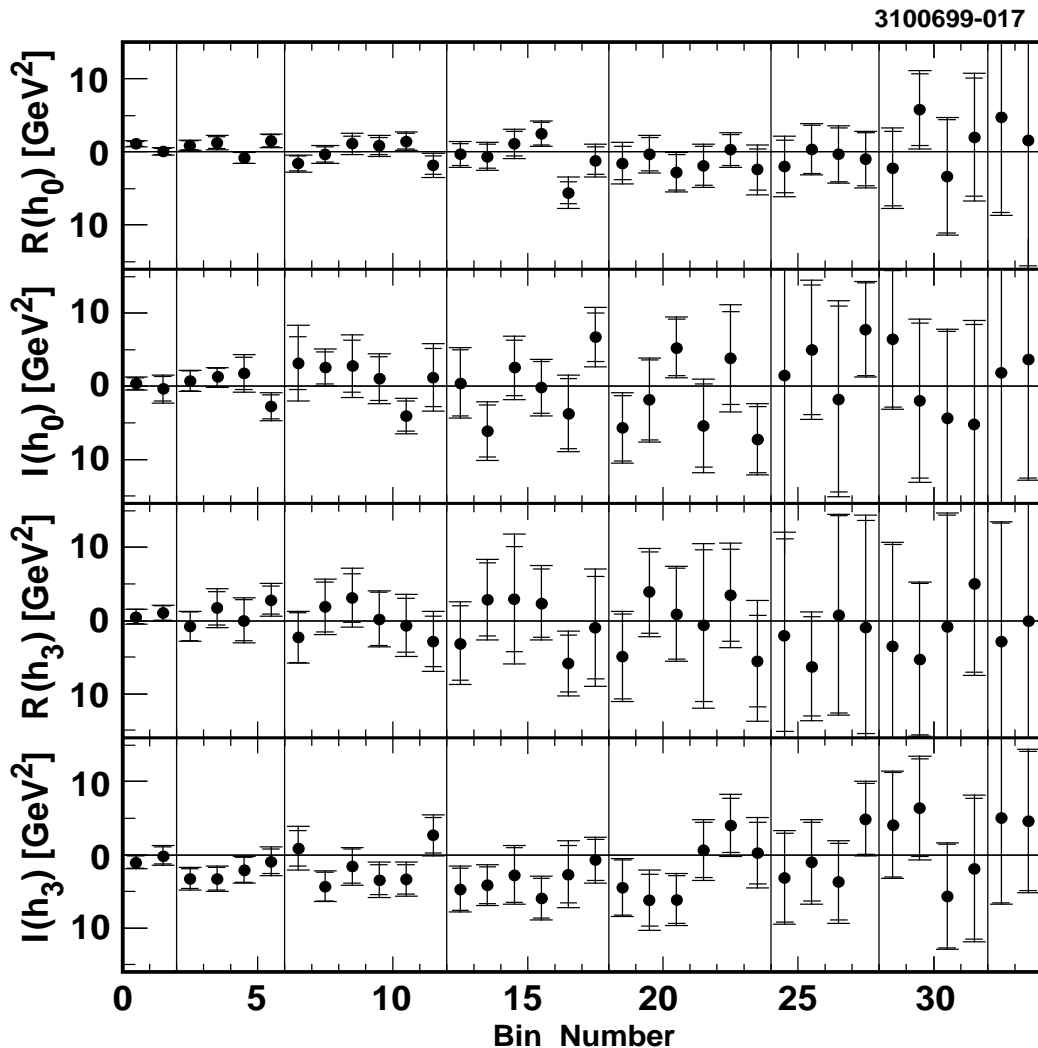


FIG. 4. The real and imaginary parts of the non-axial-vector induced components of the hadronic current as measured in our fits differential in the Dalitz plot. For further explanations see comments in caption for Fig. 3.

where the first error is statistical and the second error systematic. The individual contributions to the systematic error are: $\pm 0.29\%$ due to efficiency, $\pm 0.06\%$ due to Monte Carlo statistics, $\pm 0.03\%$ due to the energy scale of the photons, and $\pm 0.01\%$ due to background. With this we obtain the following upper limit

$$\frac{\mathcal{B}(\tau^\mp \rightarrow S\nu \rightarrow \pi^\mp \pi^0 \pi^0 \nu)}{\mathcal{B}(\tau^\mp \rightarrow \pi^\mp \pi^0 \pi^0 \nu)} < 9.4\% \text{ at } 95\% \text{ CL.} \quad (10)$$

Using the measured contributions of the vector components $\Re(h_3)$ and $\Im(h_3)$ we measure the branching ratio for vector contributions to be

$$\frac{\mathcal{B}(\tau^\mp \rightarrow V\nu \rightarrow \pi^\mp \pi^0 \pi^0 \nu)}{\mathcal{B}(\tau^\mp \rightarrow \pi^\mp \pi^0 \pi^0 \nu)} = (4.2 \pm 1.9 \pm 0.2)\%, \quad (11)$$

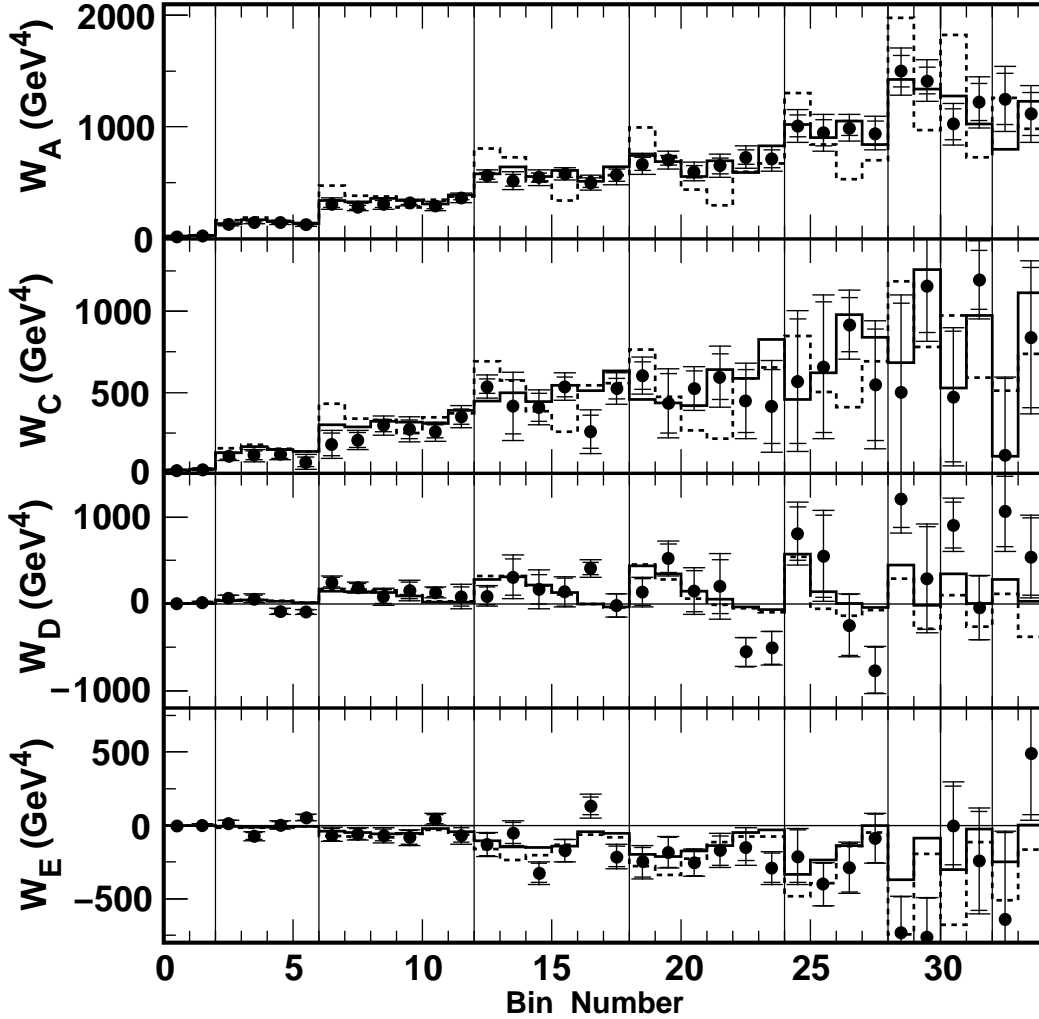


FIG. 5. The axial-vector induced structure functions W_A , W_C , W_D , and W_E as obtained from our fits to the real and imaginary parts of the hadronic current. For further explanations see comments in caption for Fig. 3.

where the first error is statistical and the second error systematic. The systematic error is given by the quadratic sum of a $\pm 0.15\%$ contribution due to efficiency, a $\pm 0.10\%$ contribution due to Monte Carlo statistics, a $\pm 0.02\%$ contribution due to the energy scale of the photons, and a $\pm 0.01\%$ contribution due to background. The upper limit on vector contributions is

$$\frac{\mathcal{B}(\tau^\mp \rightarrow V\nu \rightarrow \pi^\mp \pi^0 \pi^0 \nu)}{\mathcal{B}(\tau^\mp \rightarrow \pi^\mp \pi^0 \pi^0 \nu)} < 7.3\% \text{ at } 95\% \text{ CL.} \quad (12)$$

Combining the results on the scalar and vector components of the hadronic current we obtain the following branching ratio for non-axial-vector contributions

$$\frac{\mathcal{B}(\tau^\mp \rightarrow \text{Non-Axial } \nu \rightarrow \pi^\mp \pi^0 \pi^0 \nu)}{\mathcal{B}(\tau^\mp \rightarrow \pi^\mp \pi^0 \pi^0 \nu)} = (9.4 \pm 4.4 \pm 0.4)\%, \quad (13)$$

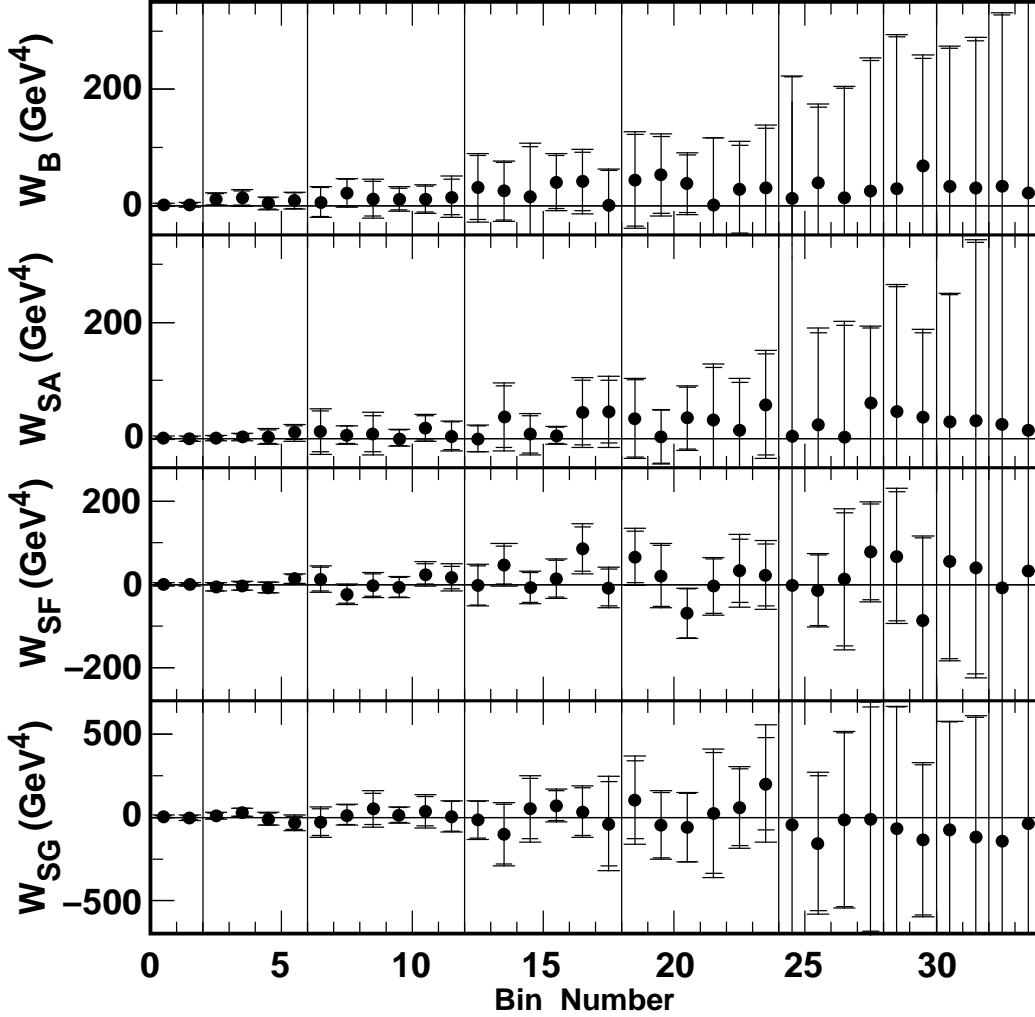


FIG. 6. The non-axial-vector induced structure functions W_B , W_{SA} , W_{SF} , and W_{SG} as obtained from our fits to the real and imaginary parts of the hadronic current. For further explanations see comments in caption for Fig. 3.

where the first error is statistical including the correlations between the vector and scalar contributions and the second error systematic. The systematic error is given by the quadratic sum of the systematic error of $\pm 0.30\%$ from the scalar contribution and the systematic error of $\pm 0.18\%$ from the vector contribution. The upper limit on non-axial-vector contributions is

$$\frac{\mathcal{B}(\tau^\mp \rightarrow \text{Non-Axial } \nu \rightarrow \pi^\mp \pi^0 \pi^0 \nu)}{\mathcal{B}(\tau^\mp \rightarrow \pi^\mp \pi^0 \pi^0 \nu)} < 16.6\% \text{ at } 95\% \text{ CL.} \quad (14)$$

The corresponding upper limit obtained by the OPAL collaboration [5] is

$$\frac{\Gamma^{\text{non-AV}}(\tau^- \rightarrow \pi^- \pi^- \pi^+ \nu)}{\Gamma^{\text{tot}}(\tau^- \rightarrow \pi^- \pi^- \pi^+ \nu)} < 26.1\% \text{ at } 95\% \text{ CL.} \quad (15)$$

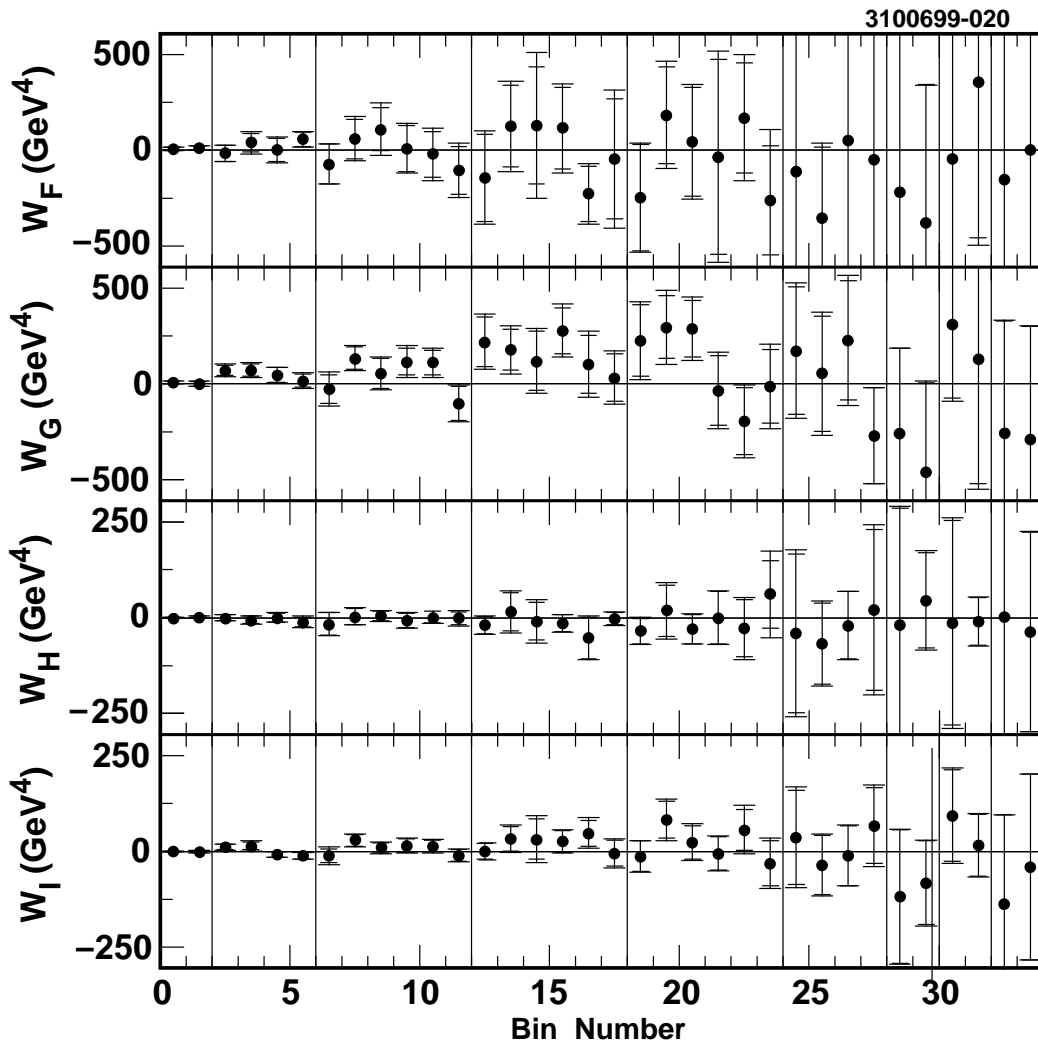


FIG. 7. The structure functions W_F , W_G , W_H , and W_I — induced by the interference between the vector and axial-vector components of the hadronic current — as obtained from our fits to the real and imaginary parts of the hadronic current. For further explanations see comments in caption for Fig. 3.

VII. SYSTEMATIC ERRORS

We consider the following sources of systematic errors:

- Overall Normalization: As mentioned in section IV, we normalize our likelihood to the world average branching ratio of $\mathcal{B}(\tau^\mp \rightarrow \pi^\mp \pi^0 \pi^0 \nu_\tau) = (9.15 \pm 0.15)\%$. The error on the branching ratio results in an overall systematic error of our normalization. In addition, the extrapolation of our measurement into the regions $Q^2 < 0.5 \text{ GeV}^2/c^4$ and $Q^2 > 2.75 \text{ GeV}^2/c^4$, *i.e.* the uncertainty on f_{sel} in Eq. 7, also yields an error on our normalization. We conservatively estimated this error to be as large as the error on the branching ratio. Accordingly, we have an overall systematic error on all structure functions of 3% and, in case of the hadronic

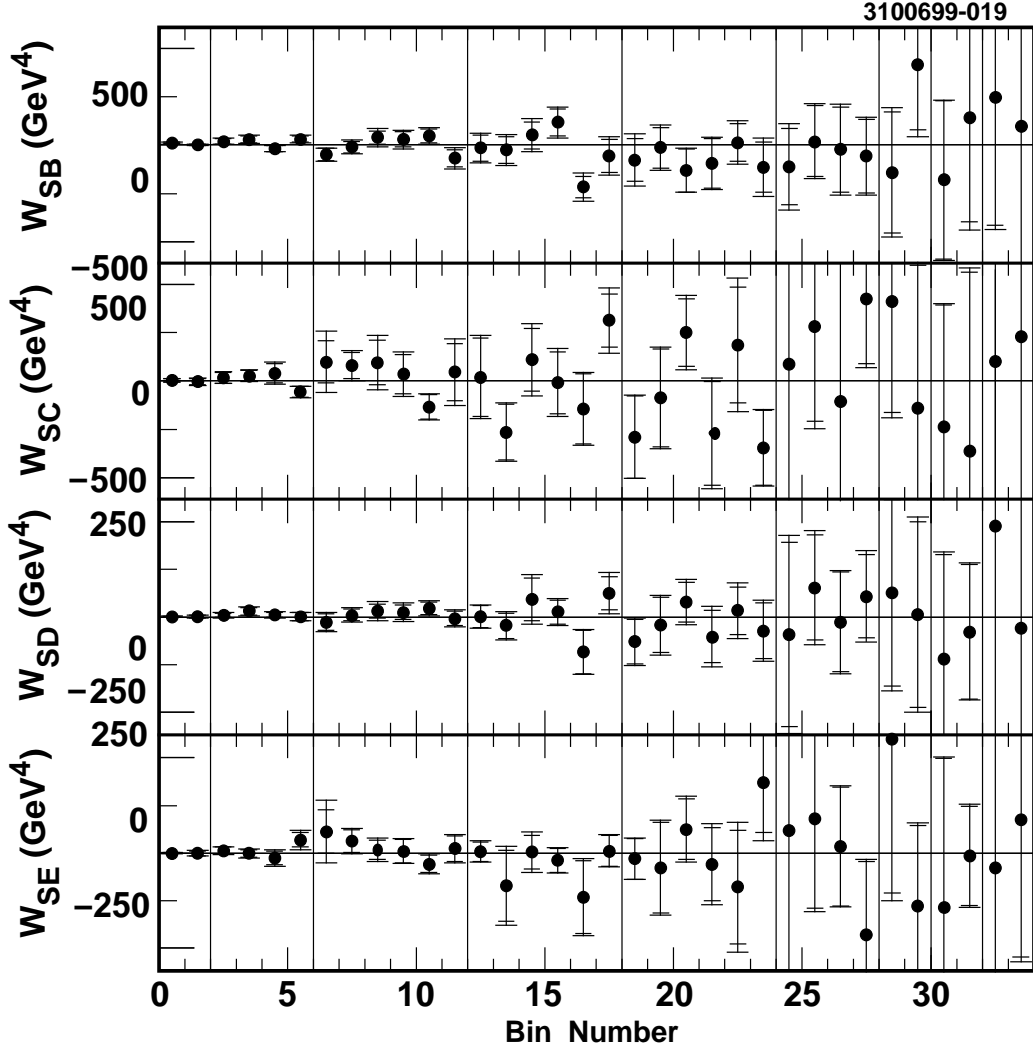


FIG. 8. The structure functions W_{SB} , W_{SC} , W_{SD} , and W_{SE} — induced by the interference between the scalar and axial-vector components of the hadronic current — as obtained from our fits to the real and imaginary parts of the hadronic current. For further explanations see comments in caption for Fig. 3.

current components, an overall systematic error of 1.7%.

- Monte Carlo Statistics: The limited statistics in the calculation of the normalization integrals of the likelihood function for the different bins in Q^2 as well as in (Q^2, s_1, s_2) results in a systematic error of our measurement. We estimated this error by subdividing our Monte Carlo sample, which has approximately ten times the size of our data sample, in six independent sub-samples. The variation in the fit results obtained are used as an estimate for this error.
- Efficiency: The not fully accurate detector simulation of the efficiency of the momenta of the three pions and the angle between the pions as well as the invariant mass of the three pions can also effect our measurement. We estimate this uncertainty by reweighting our events as

a function of the momenta of the three pions, the angle between the pions, and the invariant mass of the three pions. Since our likelihood is normalized to the world average branching ratio [14], the error in the overall efficiency does not affect our measurement. Accordingly, we only account for relative changes of the efficiency.

- **Background:** The amount of background as well as the background models used in the likelihood have uncertainties. The systematic error associated with these uncertainties have been estimated by varying in the likelihood function the background contribution and, in case of the four pion background, also the model, *i.e.* (1) $\rho(1450) \rightarrow \rho\sigma$, (2) $\rho(1450) \rightarrow a_1\pi$, and (3) combinations thereof (see section IV).
- **Photon Energy Scale:** The energy scale of the photons that form the neutral pions has an uncertainty of around 0.3%. The resulting systematic uncertainty in our measurement has been estimated by rescaling the energies of the neutral pions by 0.3% and refitting our data.

In addition to the systematic uncertainties listed above, we also have an uncertainty due to the finite detector resolution. Refitting our events including the error matrix on the charged track and the photons (scaled by a factor of four) showed that this source is negligible compared to the other sources and has, therefore, not been taken into account. This coincides with our findings of our model dependent analysis [4].

In general all five sources result in systematic errors that have roughly the same order of magnitude. However, the errors due to the overall normalization and the Monte Carlo statistics yield the largest systematic uncertainty for most of the bins.

The systematic errors obtained are shown in Figs. 2, 3, 4, 5, 6, 7, and 8 as extension to the error bars.

VIII. SUMMARY

We have measured the integrated structure functions w_A , w_C , w_D , and w_E . In addition, we determine the seven non-trivial real and imaginary components of the hadronic current in bins of (Q^2, s_1, s_2) . The results obtained on the hadronic current enable us to determine all sixteen structure functions W_X differential in the Dalitz plot. No significant non-axial-vector contributions have been found.

IX. ACKNOWLEDGEMENTS

We gratefully acknowledge the effort of the CESR staff in providing us with excellent luminosity and running conditions. J.R. Patterson and I.P.J. Shipsey thank the NYI program of the NSF, M. Selen thanks the PFF program of the NSF, M. Selen and H. Yamamoto thank the OJI program of DOE, J.R. Patterson, K. Honscheid, M. Selen and V. Sharma thank the A.P. Sloan Foundation, M. Selen and V. Sharma thank the Research Corporation, F. Blanc thanks the Swiss National Science Foundation, and H. Schwarthoff and E. von Toerne thank the Alexander von Humboldt Stiftung for support. This work was supported by the National Science Foundation, the U.S. Department of Energy, and the Natural Sciences and Engineering Research Council of Canada.

REFERENCES

- [1] ARGUS Collaboration, H. Albrecht *et al.* , Z. Phys. C **58**, 61 (1993).
- [2] ARGUS Collaboration, H. Albrecht *et al.* , Phys. Lett. B **349**, 576 (1995).
- [3] DELPHI Collaboration, P. Abreu *et al.* , Phys. Lett. B **426**, 411 (1998).
- [4] CLEO Collaboration, D. M. Asner *et al.* , CLNS 99/1601, *submitted to Physical Review D*.
- [5] OPAL Collaboration, K. Ackerstaff *et al.* , Z. Phys. C **75**, 593 (1997).
- [6] J. H. Kühn and E. Mirkes, Z. Phys. C **56**, 661 (1992) and *Erratum* Z. Phys. C **67**, 364 (1995).
- [7] E. Mirkes and R. Urech, hep-ph/9702382 (1997).
- [8] ARGUS Collaboration, H. Albrecht *et al.* , Phys. Lett. B **349**, 576 (1995).
- [9] CLEO Collaboration, M. Artuso *et al.* , Phys. Rev. Lett. **69**, 3278 (1992).
- [10] ALEPH Collaboration, D. Buskulic *et al.* , CERN-PPE/96-103 (1996).
- [11] CLEO Collaboration, Y. Kubota *et al.* , Nucl. Inst. Meth. **A320**, 66 (1992).
- [12] F. A. Behrends and R. Kleiss, Nucl. Phys. **B 177**, 237 (1981).
- [13] J. H. Kühn and A. Santamaria, Z. Phys. C **48**, 445 (1990).
- [14] Particle Data Group, C. Caso *et al.* , Eur. Phys. J. C **3**, 1 (1998).